

# The influence of filament temperature and oxygen concentration on tungsten oxide nanostructures by hot filament metal oxide deposition

J Lou<sup>1</sup>, B J Ye<sup>1</sup>, H M Weng<sup>1</sup>, H J Du<sup>1</sup>, Z B Wang<sup>2</sup> and X P Wang<sup>3</sup>

<sup>1</sup> Department of Modern Physics, University of Science and Technology of China, Hefei 230026, People's Republic of China

<sup>2</sup> Department of Applied Chemistry, Harbin Institute of Technology, Harbin 150001, People's Republic of China

<sup>3</sup> Department of Physics, University of Puerto Rico, PO Box 23343, San Juan PR 00931, USA

Received 26 March 2008, in final form 22 May 2008

Published 11 July 2008

Online at [stacks.iop.org/JPhysD/41/155410](http://stacks.iop.org/JPhysD/41/155410)

## Abstract

Tungsten oxide ( $\text{WO}_x$ ) nanostructures were prepared by a hot filament chemical vapour deposition system and the temperature of the hot tungsten filaments was changed by steps of degrees. The morphology and average growth rate were indicated by scanning electron microscopy which showed that the morphology was highly related to the filament temperature ( $T_f$ ) and the distance between the filaments and the polished Si (1 0 0) substrates ( $d_f$ ). The influence of  $T_f$  on the crystalline nature was studied by x-ray diffraction and Raman spectroscopy. The evolution of stoichiometry and types of defects was indicated by x-ray photoelectron spectroscopy and slow positron implantation spectroscopy. When  $T_f$  was up to 1750 °C, tungsten oxide nanostructure was synthesized. A turning point of  $T_f$  was found at which the nature of crystallinity and of stoichiometry was the best. As  $T_f$  increased to 2100 °C or  $d_f$  decreased, the film crystallinity decreased; correspondingly, the component ratio of stoichiometry  $\text{WO}_3$  decreased and lots of vacancy agglomerates were present. In order to develop the chemical phase from substoichiometry to stoichiometry, the oxygen gas concentration in the mixture gas during deposition should be raised to an appropriate level.

## 1. Introduction

Tungsten oxide material has attracted much attention for its excellent electrochromic and photochromic properties. It shows enormous potential for switchable windows [1], catalysts [2], lithium batteries [3] and electrochromic materials [4, 5]. Recently, interest in nanostructured tungsten oxide has been focused on use in gas sensors due to its properties of high surface-to-volume ratio, high sensitivity, fast response time and room temperature operation [6, 7]. Tungsten oxide thin films can be prepared by physical and chemical methods. In this report, tungsten oxide ( $\text{WO}_x$ ) films were prepared by using hot filament metal oxide deposition (HFMOD) in a hot filament chemical vapour deposition (HFCVD) system which is simple, cheap, catalyst free and repeatable [8, 9]. To prepare a series of samples under different conditions, the temperature of the hot tungsten filaments was varied from 1350

to 2100 °C in steps of degrees. Another series of samples was prepared with different oxygen gas concentrations (OGCs). Scanning electron microscopy (SEM), x-ray diffraction (XRD) and Raman spectroscopy were employed to characterize the as-prepared samples. Transmission electron microscopy (TEM), x-ray photoelectron spectroscopy (XPS) and slow positron implantation spectroscopy (SPIS) were also used to analyse the influence of deposition conditions on the samples.

## 2. Experimental details

The tungsten oxide nanostructures were prepared by a HFCVD system. Five clean tungsten filaments ( $\Phi = 0.5$  mm) were arrayed as vapour and heating source and the scale of the filament array was 50 mm  $\times$  20 mm. The polished Si (1 0 0) substrates were ultrasonically washed with alcohol and acetone. The distance between the filaments and the silicon

substrates was 6 mm, while the last sample was changed to 3 mm. The vacuum chamber was first pumped to  $3.5 \times 10^{-2}$  Torr. Then, high purity argon gas was fed into it. The gas pressure inside the chamber was maintained at 0.8 Torr and the flow rate of argon gas was 5 sccm ( $1 \text{ sccm} = 1.27 \times 10^{-2} \text{ Torr l s}^{-1}$ ). The temperature of the hot tungsten filaments was monitored by an infrared ray pyrometer. In a series of experiments, the oxygen level was the same, but  $T_f$  was maintained at different points because the factors working directly on the growth of tungsten oxide nanostructures such as the tungsten oxide species saturation near the substrate, substrate temperature and temperature gradient between the hot filaments and substrates were all determined by  $T_f$  [10]. The deposition might be explained by the vapour–solid (VS) model [11]. The details of each deposit are shown in table 1.

Another major factor was the deposition gas in the chamber. So in a second series of experiments, OGC in the mixture gas was maintained at different levels by another HFCVD system. Molybdenum (Mo) wafer was used as the deposition substrate. After placing the substrate, the chamber was pumped down to  $2.0 \times 10^{-5}$  Torr. Three kinds of gas mixture, 8.7% of  $\text{CH}_4$ , 0.3% of  $\text{O}_2$ , 91% of  $\text{H}_2$  (low-OGC); 8.5% of  $\text{CH}_4$ , 0.5% of  $\text{O}_2$ , 91% of  $\text{H}_2$  (medium-OGC) and 8.3% of  $\text{CH}_4$ , 0.7% of  $\text{O}_2$ , 91% of  $\text{H}_2$  (high-OGC), were used. The flow rate of mixed gas was 5 sccm. The gas pressure inside the chamber was maintained at 0.5 Torr and  $T_f = 2400^\circ\text{C}$  during the deposition for 60 min.

The SEM and TEM images were taken with a FEI Sirion200 working at 5 kV and JEOL JEM 2010. XRD analysis was measured in the transmission mode by a PHILIPS X PERT Pro with a Cu  $K\alpha$  anode and an angular resolution of  $0.03^\circ$ . Raman spectra were recorded using an excitation wavelength corresponding to the 514.5 nm of an Ar ion laser by a JY LABRAM-HR. The power was less than 1 mW and the scan time was 60 s in order to prevent damage to the samples.

**Table 1.** Preparation parameters of the series of samples.

Sample	Deposition time (min)	Power (W)	$T_f$ ( $^\circ\text{C}$ )	$d_f$ (mm)
1350	30	50	1350	6
1550	30	80	1550	6
1650-10min	10	100	1650	6
1750	30	150	1750	6
1900	30	180	1900	6
2100	30	260	2100	6
2100-3mm	25	260	2100	3

XPS analysis was accomplished by Thermo-VG Scientific ESCALAB 250. An AVANTAGE fitting program developed by Thermo Electron Corp. was used to decompose the spectra.

The samples were analysed by using a slow positron beam device that can be applied to defect studies of thin films. The positrons, generated by the decay of radioactive source  $^{22}\text{Na}$ , were transmitted by a magnetic confinement vacuum tube system, and focused. The output energy of the positron beam at the end was 24 eV and the beam spot size was less than 8 mm. The beam strikes the samples at the bottom. The energy of the positrons ( $E$ ), namely the injection depth of them, could be changed by adjusting the negative high voltage added to the sample stage. 511 keV annihilation photons were detected by the system of high purity germanium (ORTECGEM-1075). The  $S$  and  $W$  parameters describe the spectrum of the annihilation photons. The  $S$  parameter, the ratio of the counts in the regional centre near the summit of 511 keV to the total counts, revealed the electron momentum density at low momentum of the materials. The  $W$  parameter, the ratio of the counts in the two wings of the spectrum to the total counts, provided the electron momentum density at high momentum of the materials. An increase in positrons trapping to vacancy-related defects resulted in a narrowing of the spectrum, and an increased  $S$  parameter. The same occurred if the size of the open volume of the positron trapping defects increased [12].

### 3. Results and discussion

#### 3.1. First series of samples

Figures 1 and 2 show, respectively, a series of plan-view and cross-section-view SEM images of the deposits. When  $T_f = 1350^\circ$  and  $1550^\circ\text{C}$ , only thin films similar to those in figures 1(a) and (b) are observed. The film was smoother at  $T_f = 1550^\circ\text{C}$ . Nanostructures were formed with the increment of  $T_f$ . As shown in figure 2, a distinguishable trend of the deposits is observed as  $T_f$  increases. Figure 2(a) shows that only a compact film about  $3 \mu\text{m}$  grew on the substrate at  $T_f = 1550^\circ\text{C}$ . Figure 2(b) shows  $4.82 \mu\text{m}$  high nanobundles with widths of about 300 to 400 nm over  $5.79 \mu\text{m}$  thick film at  $T_f = 1750^\circ$ . Each nanobundle seems to be flat, and some nanobundles ramify, which could improve the surface-to-volume ratio. Figure 2(c) shows  $6.38 \mu\text{m}$  high nanobundles with widths of about 500 nm over a  $2.14 \mu\text{m}$  thick film at  $T_f = 1900^\circ\text{C}$ . Figure 2(d) also shows nanobundles with a larger width of about  $1 \mu\text{m}$  and a height of about  $4.5 \mu\text{m}$  over

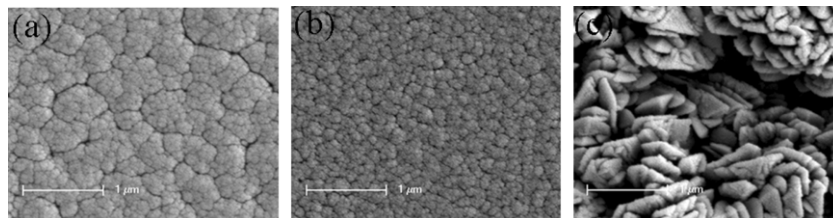


**Figure 1.** Plan-view SEM images of deposits prepared at different filament temperatures of (a)  $1350^\circ\text{C}$ , (b)  $1550^\circ\text{C}$  and (c)  $1750^\circ\text{C}$ . The scale bar is  $1 \mu\text{m}$ .

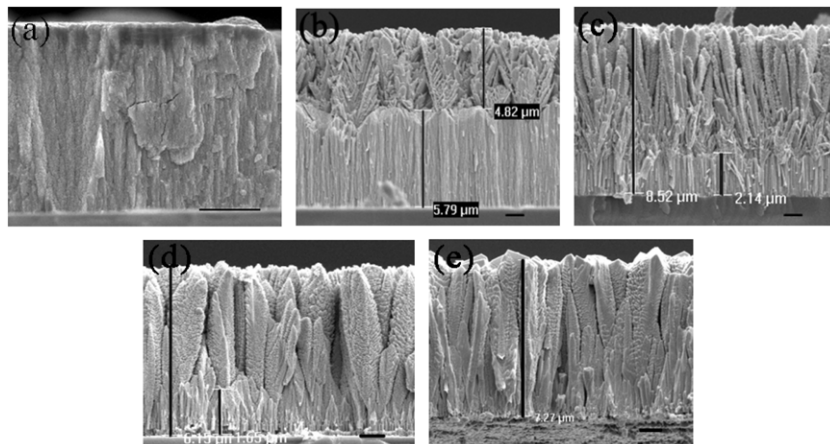


**Figure 2.** Cross-section-view SEM images of the nanostructures grown on Si (100) substrates at different filament temperatures of (a) 1550°C, (b) 1750°C, (c) 1900°C and (d) 2100°C. (e) Morphologies of the deposit 2100-3 mm and the layer of nanostructures are separated from the silicon substrate. The scale bar is 1 μm.

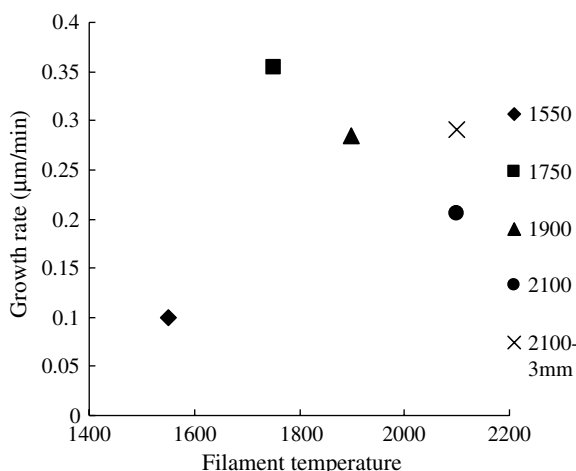


**Figure 3.** Variation of growth rate of tungsten oxide on Si (100) substrates at different  $T_f$  and  $d_f$ .

a 2.15 μm thick film. The image of sample 2100-3 mm is presented in figure 2(e). They are also nanobundles, but more compact, with a width of about 1 μm and a height of about 7.27 μm and no film below. When  $T_f$  was up to 1750°C or kept at higher values, tungsten oxide nanostructures were synthesized. The height of the nanobundles became larger as  $T_f$  increased. In contrast, the thickness of the tungsten oxide film became smaller as  $T_f$  increased. When  $T_f = 2100°C$  but  $d_f$  decreased, the height of the nanobundles became larger, so did the growth rate. From figure 2, the average growth rates of tungsten oxide on the Si (100) substrates at different  $T_f$  and  $d_f$  are identified as shown in figure 3. The growth rate was lowest when  $T_f$  was correspondingly lower at 1550°C, which may be due to the low density of tungsten oxide species. When  $T_f = 1750°C$ , the growth rate was maximum. As  $T_f$  kept increasing, the growth rate decreased, which might be due to the increase in the sublimation rate/vapour pressure of the deposited tungsten oxide at higher temperatures [13, 14].

XRD patterns shown in figure 4 identify the crystalline structure of the tungsten oxide films. Sample 1650-10 min is

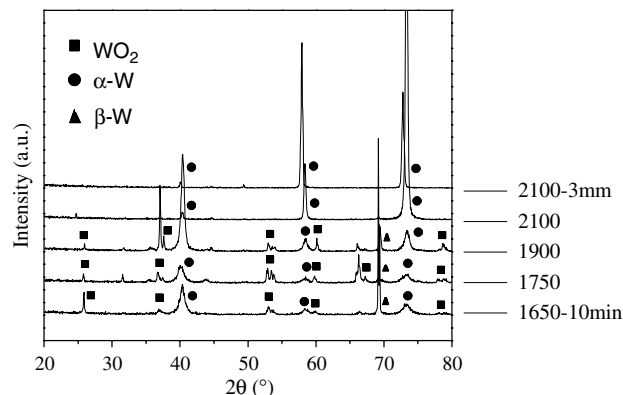


**Figure 4.** XRD patterns for tungsten oxide on Si (100) substrates at different  $T_f$  and  $d_f$ .

predominantly crystalline  $WO_2$  (JCPDS 86-0134). The peaks of  $\alpha$ -W and  $\beta$ -W are detected clearly [15]. The XRD spectra of samples 1750 and 1900 have similar results, and there exist three weak peaks at  $2\theta$  diffraction angles between 22° and 25°, which might be assigned to monoclinic  $WO_3$ . The peaks of  $\alpha$ -W of sample 1750 are the weakest. With the increase in  $T_f$ , the peaks of  $\beta$ -W trail off. When  $T_f$  increases to 2100°C (samples 2100 and 2100-3 mm), the peaks of crystalline  $WO_2$  vanish, indicating that the films prepared at  $T_f = 2100°C$  are totally stable  $\alpha$ -W.

Figure 5 shows the Raman spectra of four samples that formed nanostructures. The Raman spectrum of sample 1750 exhibits Raman lines at: 360(w), 274(w), 286(s), 331(w), 347(w), 476(m), 514(s), 600(s), 619(m), 782(s)  $cm^{-1}$  (w—weak, m—medium, s—strong), which are ascribed to crystalline  $WO_2$  [16]. The Raman spectrum of sample 1900 is similar to sample 1750, but adds a Raman line at 723(w)  $cm^{-1}$ . The crystalline  $WO_3$  Raman spectrum exhibits major Raman bands at 275, 719 and 808  $cm^{-1}$ , where the 275  $cm^{-1}$  is assigned as the W–O–W bending mode and the 719 and 808  $cm^{-1}$  as the W–O–W stretching modes [17, 18]. The bands at 274, 723  $cm^{-1}$  are weak, and the 808  $cm^{-1}$  are not

clearly observed possibly due to the overlap by the  $782\text{ cm}^{-1}$  band. So crystalline  $\text{WO}_3$  might be synthesized and crystalline  $\text{WO}_2$  is dominant in the deposits prepared at  $T_f = 1750$  and  $1900^\circ\text{C}$ . Sample 2100 shows only one band in the  $786\text{ cm}^{-1}$  region. The Raman spectrum of sample 2100-3 mm indicates that the deposit is totally amorphous in nature. As  $T_f$  increases or  $d_f$  decreases, the film crystallinity decreases. The results of the Raman spectra are in agreement with the results of XRD.

During deposition, the surface of tungsten filaments first reacted with oxygen. Tungsten oxide species were evaporated from the surface and deposited on the substrate in a relatively low temperature zone. Simultaneously, the reduction progressed from  $\text{WO}_3$  to W via a wide series of reduced tungsten oxide. The stepwise reduction of  $\text{WO}_3$  over  $\text{WO}_{3-x}$  phases into  $\text{WO}_2$  and finally metallic W was reported by Schubert [19–21]. XPS was carried out to investigate the chemical states of the W and O atoms in the films of samples 1750, 1900, 2100, 2100-3 mm and 1650-10 min presented in figures 6(a)–(e). In figure 6(a), the doublet at binding energies 37.5 eV for W 4f5/2 and 35.5 eV for W 4f7/2 is prominent. It is an indication of the  $\text{W}^{6+}$  state or stoichiometric  $\text{W}_3$ . The shoulders at 31.1, 33.2 and 33.8 eV reveal the existence of substoichiometric reduced tungsten oxide probably in  $\text{W}^0$  to  $\text{W}^{5+}$  states including  $\text{W}^{4+}$  ( $\text{WO}_2$ ) and  $\text{W}^0$  (NIST XPS Database). In figure 6(b), the doublet at binding energies 37.5 eV for W 4f7/2 and 35.5 eV for W 4f5/2 is still prominent, but the shoulders at 31.1, 32.5, 33.2, 33.7 and 34.3 eV increase. Figure 6(c) is similar to

6(b), the chemical states of W are almost the same when  $T_f$  increases from 1900 to  $2100^\circ\text{C}$ . Samples 1750, 1900 and 2100 are mixtures of stoichiometric  $\text{WO}_3$  and different substoichiometric reduced tungsten oxides. As shown in figure 6(d), when  $d_f$  of sample 2100-3 mm was reduced to 3 mm, the doublet at binding energies 33.2 eV for W 4f5/2 and 31.0 eV for W 4f7/2 is prominent and shoulders at 31.8 and 33.9 eV exist. Correspondingly, the doublet for  $\text{W}^{6+}$  becomes weak but still distinguishable. Figure 6(e) shows the doublet of  $\text{W}^0$  is prominent too. To summarize, as  $T_f$  increases, the deposits go to stoichiometric [22]. And there is a turning point at about  $1750^\circ\text{C}$ . As  $T_f$  increases continuously from the turning point, substoichiometric tungsten oxide gradually dominates the deposits. When  $T_f = 2100^\circ\text{C}$  and  $d_f$  decreases, the component ratio of stoichiometric tungsten oxide decreases. XPS element and each tungsten state component quantitative results for the samples are shown in table 2.  $\text{WO}_x$  is the ratio of W (except  $\text{W}^0$ ) and O.  $\text{W}^{x+}$  is a substoichiometric reduced tungsten state, mainly  $\text{W}^{5+}$  and  $\text{W}^{4+}$ . The OGC in the gas mixture during deposition might be raised to an appropriate level to develop the chemical phase from substoichiometry to stoichiometry.

Figure 7(a) shows the  $S$ – $E$  curves that are fit performed by the program package VEPFIT. According to the formula of the mean depth  $\langle z \rangle = (36 \times E^{1.62})/\rho$ , the mean depth is between about 600 nm (implanted into pure  $\text{WO}_3$  films) and 200 nm (implanted into pure  $\alpha$ -W materials). But there exists some free space between the nanobundles, and positrons might be annihilated in the roots of the nanobundles. And the positron implantation profile at a given energy extends about twice the value of  $\langle z \rangle$  [23]. The thin films below the nanobundles completely shadow the substrates. All the films are thicker than 1200 nm, and almost no positrons annihilated in the Si substrates. The measured  $S$  value of all samples first continuously decreases with the increase in positron energy because the positrons at low energy may diffuse to the surface and form Ps that increases the  $S$  value. The  $S$  value reaches a plateau value, which means the positrons are annihilated exclusively in the tungsten oxide films when positron energies are larger than about 5 keV (1900, 2100) or 13 keV (1550, 1650-10 min, 1750). The difference is caused by the larger  $L_{\text{eff}}$  of samples 1550, 1650-10 min and 1750 shown in figure 7(b). When  $T_f = 1550$  and  $1650^\circ\text{C}$ , the plateau value of  $S$  is the highest and decreases to the lowest at  $T_f = 1750^\circ\text{C}$ . The plateau value of  $S$  increases when  $T_f = 1900$  and  $2100^\circ\text{C}$ .

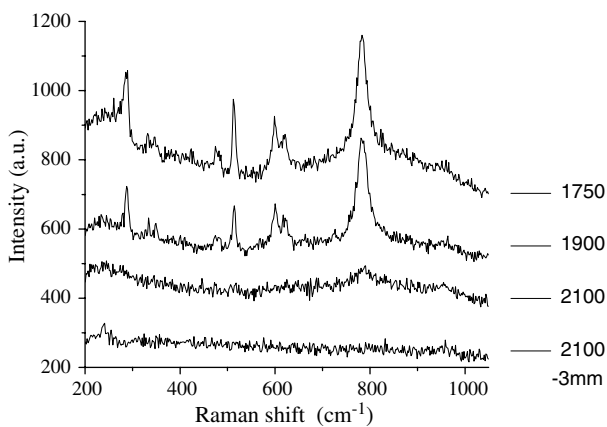


Figure 5. Raman spectra of tungsten oxide on Si (100) substrates at different  $T_f$  and  $d_f$ .

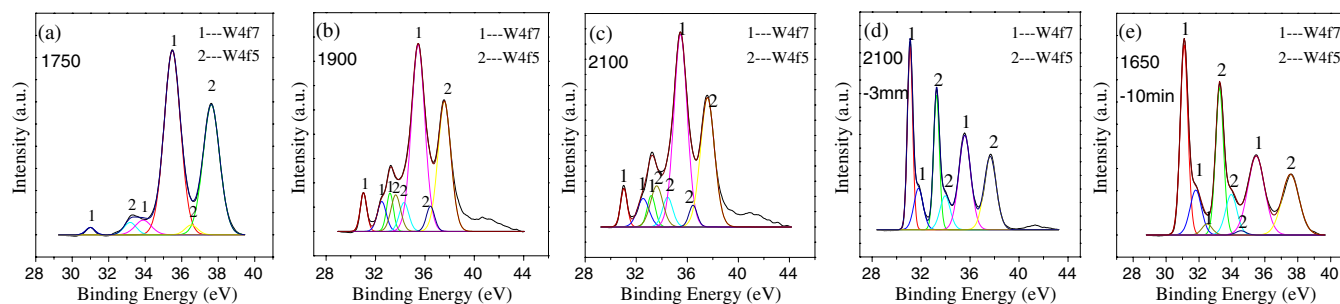


Figure 6. (a)–(e) are XPS spectra for W4f of samples 1750, 1900, 2100, 2100-3 mm and 1650-10 min.

(This figure is in colour only in the electronic version)

The content of low valence states W in sample 1650-10 min is larger than other samples and samples 1900 and 2100 take second place. When low valence states W exist in the film, the free valence electrons that do not form W–O bonds around the nucleus are still in existence because of the lack of oxygen. It is easier to form effective positron capture centres around low valence state W ions. These capture centres will increase the *S* value. And the bound energies of valence electrons of stoichiometric W<sup>6+</sup> are distinctly higher than those of low valence states of W [24]. The *S* value is dependent on the chemical state of tungsten and defect concentration and the size revealed by *L*<sub>eff</sub>. The results of the *S*–*E* curves coincide with that of XPS, namely the *S* value coincides with the component ratio of substoichiometric W<sup>x+</sup>, which is shown in figure 7(c). It is deduced that the ratios of W<sup>x+</sup> of samples 1550 and 1650-10 min are similar because *L*<sub>eff</sub> of them are similar. The *L*<sub>eff</sub> of samples 1900 and 2100 are 8.59 ± 1.18 and 6.57 ± 0.50 nm, respectively, illuminating that the highly defective films present a large number of vacancy agglomerates.

**Table 2.** XPS element and each tungsten state components: quantitative results for 1650-10 min, 1750, 1900, 2100 and 2100-3 mm.

	1650-10 min	1750	1900	2100	2100-3 mm
W (at%)	69.97	50.61	57.27	59.77	69.06
O (at%)	30.03	49.39	42.73	40.23	30.94
W <sup>6+</sup> (at%)	38.64	89.90	71.92	70.28	45.04
W <sup>x+</sup> (at%)	18.55	3.82	19.14	21.42	16.32
W <sup>0</sup> (at%)	42.81	6.28	8.94	8.30	38.64
WO <sub>x</sub>	WO <sub>0.75</sub>	WO <sub>1.04</sub>	WO <sub>0.82</sub>	WO <sub>0.73</sub>	WO <sub>0.73</sub>

The variation of the types of defects is revealed by the *S*–*W* plots. As shown in figure 7(d), *S*–*W* points would be on one straight line if only one type of defect existed in the materials. The fitted straight lines of the samples slope with increasing *T*<sub>f</sub> gradually (slope = –0.303 07, –0.340 87, –0.378 24, –0.404 73 for *T*<sub>f</sub> = 1550 °C, 1750 °C, 1900 °C, 2100 °C, respectively), which indicates that the ratio of oxygen vacancies increases with *T*<sub>f</sub>. Oxygen vacancies are not positron capture centres, but would scatter the positrons that decrease the diffusing length. The *S*–*W* plot of sample 1650-10 min, only 10 min deposited, is presented in figure 7(e), which is different from other samples. There is no straight line between the *S* and *W* points, which suggests a different surface layer about 30 nm was synthesized. In this layer the concentration of oxygen vacancies is drastically lower, indicating a new deposit surface not completely deoxidized by hydrogen or any other gas. The component ratio of stoichiometric tungsten oxide is expected to be high in the layer. Positron annihilation spectra analysis further demonstrates that the nature of crystallinity and of stoichiometry is the best and the defect concentration is lowest at the turning point *T*<sub>f</sub> = 1750 °C because of the minimal plateau value of *S* and maximal *L*<sub>eff</sub>.

### 3.2. Second series of samples

Figure 8 shows the XRD pattern for the second series of samples. The low-OGC and medium-OGC samples are predominantly α-W. The XRD spectra of the high-OGC samples show that the film consists of WO<sub>3</sub>, WO<sub>2</sub> and α-W, indicating the crystalline structure of tungsten oxide altered from the amorphous structure. Figure 9 shows the TEM image

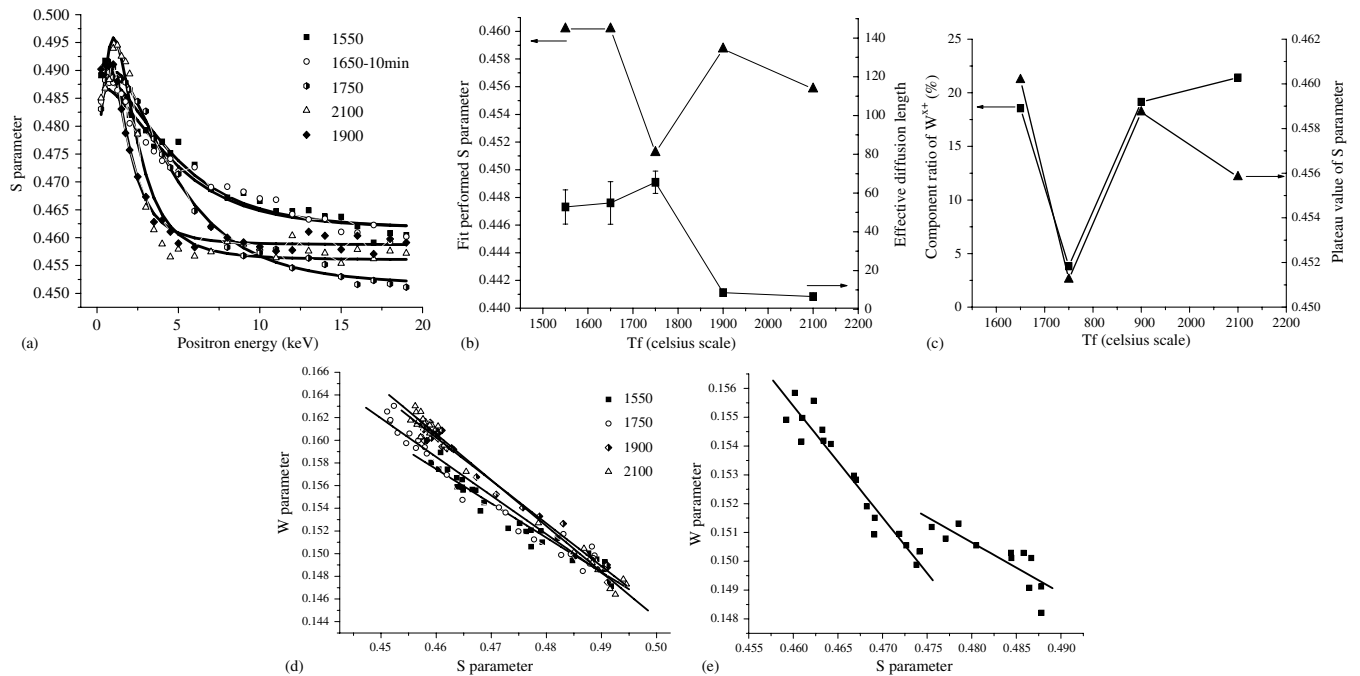


**Figure 7.** SPIS results of samples prepared at different *T*<sub>f</sub>. (a) *S*–*E* curves of samples 1550, 1650-10 min, 1750, 1900 and 2100. (b) Fit performed *S* parameter and effective diffusion length of positrons of samples 1550, 1650-10 min, 1750, 1900 and 2100. (c) Component ratio of stoichiometric W<sup>x+</sup> and plateau value of *S* versus *T*<sub>f</sub> of samples 1650-10 min, 1750, 1900 and 2100. (d) *S*–*W* plots for samples 1550, 1750, 1900 and 2100. (e) *S*–*W* plot for sample 1650-10 min.

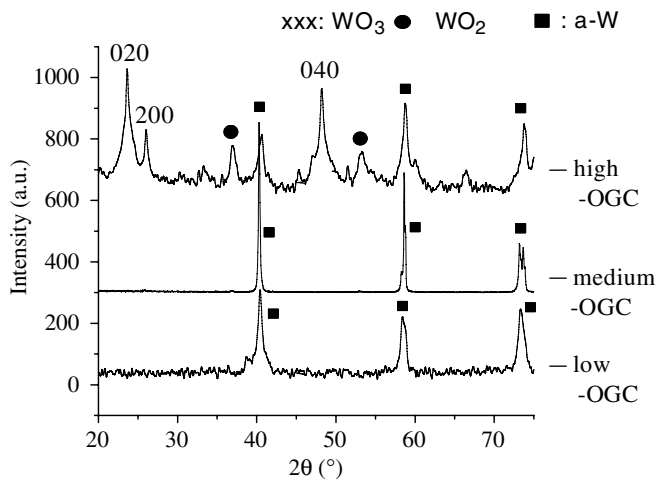


Figure 8. XRD pattern for samples at different OGCs.

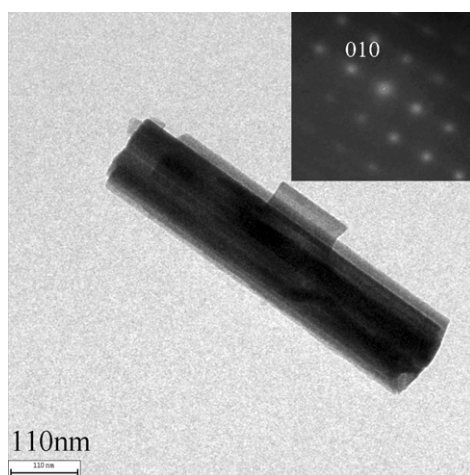


Figure 9. TEM image of high-OGC sample. The corresponding SAED pattern is shown in the inset.

and the selected area electron diffraction (SAED) pattern of the high-OGC sample, indicating the synthesis of monocrystal tungsten oxide nanorods. The nanorod grows along the orientation 0 1 0, which is in agreement with the result of XRD that the strongest peak is 0 2 0. The SEM images reported in the literature show the rise of OGC from 0.3% to 0.7%, the morphologies of the samples varied from particle-based film (low-OGC) to nanorod arrays (high-OGC) [25]. The XPS element and each tungsten state component quantitative results for samples are shown in table 3 (XPS spectra are not shown). The high-OGC sample is proximal to stoichiometric tungsten oxide. Note that a considerable amount of  $W^{6+}$  exists in the low-OGC and medium-OGC samples but the XRD patterns show only  $W^0$ . This can be explained in terms of the amorphicity of  $WO_3$  in the as-prepared samples. A high sensitivity and quick response gas sensor has been developed based on the high-OGC sample and tungsten nanorod arrays deposited on cylindrical substrates [26].

The  $S-E$  curves and the  $S-W$  plots are presented in figures 10(a) and (b). The plateau value of  $S$  of the

Table 3. XPS element and each tungsten state component quantitative results for low-OGC, medium-OGC and high-OGC samples.

	Low-OGC	Medium-OGC	High-OGC
W (at%)	58.78	45.60	38.66
O (at%)	6.72	36.41	50.63
C (at%)	34.50	17.99	10.72
$W^{6+}$ (at%)	90.90	91.28	84.08
$W^{x+}$ (at%)	7.03	4.80	4.32
$W^0$ (at%)	2.07	3.92	11.60
$WO_x$	$WO_{0.12}$	$WO_{0.80}$	$WO_{1.32}$

high-OGC sample is the lowest, and that of the low-OGC sample is the largest. The plateau value of  $S$  decreases with the increase in OGC, which also coincides with the fact that the chemical phase developed from substoichiometry to stoichiometry if OGC in the gas mixture was raised. The fit performed  $L_{eff}$  of the samples are all small, and the error of the medium-OGC sample is much too large, so the evolution of  $L_{eff}$  with OGC cannot be found. But the value of  $L_{eff}$  also reveals the existence of vacancy agglomerates in these three samples. The  $S-W$  plots show that the fitted straight lines of the sample slope gradually with decrease in  $T_f$  (slope =  $-0.35232$ ,  $-0.3616$ , and  $-0.39618$  for low-OGC, medium-OGC and high-OGC, respectively), which indicates that the ratio of oxygen vacancies increased with OGC. The oxygen quantitative component in the high-OGC sample is the largest, but the concentration of oxygen vacancies is also the highest.

#### 4. Conclusions

Two series of tungsten oxide films were prepared by HFCVD at different  $T_f$  and OGCs. In the first series of samples, tungsten oxide nanostructures were synthesized when  $T_f$  was up to  $1750^\circ\text{C}$ . A turning point was found at  $T_f = 1750^\circ\text{C}$  where the nature of crystallinity and of stoichiometry was the best and the defect concentration was the lowest. As  $T_f$  increased continuously or  $d_f$  decreased, the film crystallinity decreased; correspondingly the component ratio of  $WO_3$  decreased and a large number of vacancy agglomerates was found. In the second series of samples, the chemical phase developed from substoichiometry to stoichiometry as the OGC in the mixture gas during deposition was raised to an appropriate level. The results of SPIS coincided with those of other methods. The slow positron beam system is an effective and sensitive method to identify the properties of stoichiometry and types of defects with the depth of tungsten oxide thin films. In conclusion,  $T_f$ ,  $d_f$  and OGC greatly influence the properties of deposited tungsten oxide films and nanostructures. The properties of tungsten oxide can be controlled by adjusting the deposition parameters.

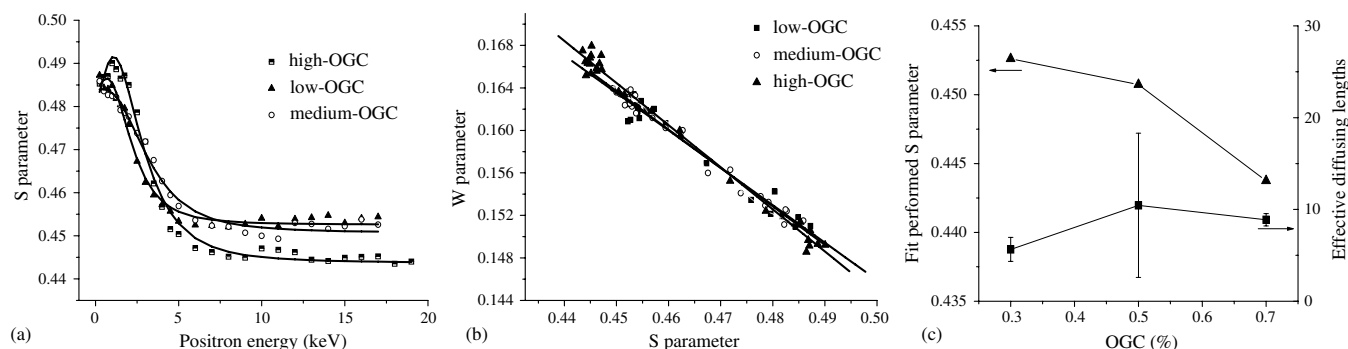


**Figure 10.** SPIS results of samples at different OGCs. (a)  $S$ - $E$  curves. (b)  $S$ - $W$  plots. (c) Fit performed  $S$  parameter and effective diffusing lengths of positrons.

## Acknowledgments

This work was supported by the National Natural Science Foundation of China (Nos 10675114 and 10675115).

## References

- [1] Georg A *et al* 2008 *Vacuum* **82** 730
- [2] Ponzi M, Duschatzky C, Carrascull A and Ponzi E 1998 *Appl. Catal. A* **169** 373
- [3] Yu A, Kumagai M, Liu Z and Lee J Y 1998 *J. Solid State Electrochem.* **2** 394
- [4] Deramare R, Gillt M, Gillt E and Guaino P 2007 *Surf. Sci.* **601** 2675
- [5] Yoo S J, Lim J W and Sung Y E 2007 *Appl. Phys. Lett.* **90** 173126
- [6] Balázsi C *et al* 2008 *J. Eur. Ceram. Soc.* **28** 913
- [7] Kim Y S *et al* 2005 *Appl. Phys. Lett.* **86** 213105
- [8] Shankar N, Yu M F, Vanka S P and Glumac N G 2006 *Mater. Lett.* **60** 771
- [9] Durrant S F *et al* 2008 *Thin Solid Films* **516** 789
- [10] Chi L F *et al* 2006 *Nanotechnology* **17** 5590
- [11] Zhou J, Deng N S, Chen J, She J C and Wang Z L 2003 *Adv. Mater.* **15** 1835
- [12] Jin S W *et al* 2004 *J. Phys. D: Appl. Phys.* **37** 1841
- [13] Patil P S, Nikam S B and Kadam L D 2001 *Mater. Chem. Phys.* **69** 77
- [14] Galléa F, Li Z C and Zhang Z J 2006 *Appl. Phys. Lett.* **89** 193111
- [15] Chen C H *et al* 2006 *Nanotechnology* **17** 217
- [16] Frey G L *et al* 2001 *J. Solid State Chem.* **162** 300
- [17] Lu Z, Kanan S and Tripp C 2002 *J. Mater. Chem.* **12** 983
- [18] Zhou L *et al* 2008 *Microporous Mesoporous Mater.* **109** 248
- [19] Ogata E, Kamiya Y and Ohta N 1973 *J. Catal.* **29** 296
- [20] Penner S *et al* 2008 *Thin Solid Films* **516** 2829
- [21] Schubert W D *et al* 1990 *Int. J. Ref. Met. Hard Mater.* **9** 178
- [22] Pal S and Jacob C 2006 *Appl. Surf. Sci.* **253** 3317
- [23] Brauer G *et al* 2007 *Nanotechnology* **18** 195301
- [24] Ma C X *et al* 2004 *Positron Annihilation: ICPA-13 Proc. (Materials Science Forum vol 445-6)* p 141
- [25] Wang X P, Yang B Q, Zhang H X and Feng P X 2007 *Nanoscale Res. Lett.* **2** 405
- [26] Wang X P, Lou J, Wang Z B and Feng P 2008 *MRS Spring Meeting (California, USA)* 1080-O15-18